TASK Quarterly 26 (2) 2022

A Mean-Line Flow Model of Viscous Liquids in a Vortex Pump

Wenguang Li
School of Energy and Power Engineering
Lanzhou University of Technology, Lanzhou 730050, China
Email: Liwg43@163.com

Date: 18 May 2023

Abstract

The axial, radial and tangential velocity profiles of six fluids were extracted from computational fluid dynamics simulation results at points in a pump chamber 1 mm distant from the blades in a vortex pump at the specific speed of 76. The critical radius was specified in the axial velocity radial profiles to determine the impeller inlet and outlet at six viscosities and part-load, design, and over-load points. A mean-line flow model and hydraulic loss model were built from the profiles. The incidence, incidence loss in the inlet, deviation angle, and slip factor in the outlet were calculated. The impeller theoretical head, pump hydraulic efficiency and volumetric efficiency were analyzed. It was shown that the axial, radial and tangential velocity profiles relate closely to the flow rate as usual, but also the viscosity, especially at low flow rates and in the inlet. The low flow rate and viscosity lead to near zero axial and radial velocities, a faster tangential velocity than the blade speed, negative incidence, and a small incidence loss coefficient in the inlet. The dimensionless critical radius ranged within 0.77–0.89 and reduces with the increasing flow rate and viscosity. The mean slip factor is between 0.11 and 0.20 and rises with the increasing flow rate and viscosity. The mean incidence loss coefficient is within 0.0020–0.15 and augments with the increasing flow rate but increases with the decreasing viscosity under part-load conditions. The theoretical head estimated by using the fluid tangential velocity between the outlet of the impeller and the inlet of the chamber is more reasonable.

Keywords:

vortex pump; mean-line flow model; viscosity; slip factor; incidence; deviation angle

https://doi.org/10.34808/81j7-9s94

Nomenclature

A_1 area of the inlet of a channel in the impeller, m^2
A_2 area of the outlet of a channel in the impeller, m^2
a_1 blade pitch in the inlet of a channel in the impeller, mm
a_2 blade pitch in the outlet of a channel in the impeller, mm
a_4 depth of the nozzle in the volute, mm
B width of the pump chamber, mm
b_3 volute width, mm
b_4 width of the nozzle in the volute, mm
$C_{1\varepsilon}$, $C_{2\varepsilon}$ model constants in the ε transport equation Eq.(A4)
C_μ constant in the turbulence eddy viscosity μ_t expression in the standard $k-\varepsilon$ two-equation model
$D2$ impeller outer diameter, mm
d hydraulic diameter, m
E turbulence constant in wall function Eq.(A5)
e_x unit length of the x-coordinate which is along the pump shaft axis
G_k production of turbulence kinetic energy in Eq.(A3) and (A4), W/m^3
g acceleration due to gravity, $g = 9.81$ m/s^2
H head of the vortex pump, m
h hydraulic loss in the vortex pump, m
k turbulent kinetic energy, m^2/s^2
L length of the nozzle, mm
N number of the points employed to extract the fluid velocity profiles
n impeller rotational speed of the vortex pump, r/min
n_s specific dynamic speed of the vortex pump, $n_s = \frac{3.65n\sqrt{Q}}{H^{3/4}}$ (r/min, m^3/s, m)
p local static pressure of fluid, Pa
Q flow rate in the vortex pump, m^3/h
q leakage flow rate of the fluid, m^3/h
R radial coordinate, mm
r dimensionless radial coordinate, $r=R/R_2$
R_2 impeller outer radius, $R_2 = 0.5\ D_2$
R_3 base circle radius of the volute, mm
R_4 volute radius, mm
R impeller Reynolds number, $R\left(\frac{\pi n}{30}\right)\left(\frac{D_2}{2}\right)\left(\frac{D_2}{2}\right)\left(\frac{1}{\nu}\right)$
t time, s
u_i, u_j time-averaged velocity of fluid, m/s
u blade speed in the vortex pump, $u = \omega R$, m/s
v dimensionless absolute velocity of fluid, $v = V/u$ V absolute velocity of fluid, m/s
W relative velocity of fluid in the impeller, m/s
x_i, x_j Cartesian coordinates in i and j directions, i and j are the coordinate direction index, $i,j = 1,2,3$ in a flow field
y distance from the first mesh layer node to a wet solid wall, m
y_b physical viscous sub-layer thickness, mm

Greek

α expansion angle of a channel in the impeller, °
β flow angle measured from the reverse direction of impeller rotation, °
β_b blade angle measured from the reverse direction of impeller rotation, °
ΔV_u incidence velocity loss in the inlet or slip velocity in the outlet, m/s
$\Delta\beta$ incidence or deviation angle of flow, °
δ blade metal thickness, mm
ε turbulent dissipation, m^2/s^3
Z number of blades
η efficiency of the vortex pump
θ_v warp angle of the volute body, °
κ von Karman constant in wall function Eq.(A5)
λ friction factor
μ dynamic viscosity of fluid, $\mu = \rho\nu$, Pa s
ν kinematic viscosity of fluid, cSt or m^2/s
ρ density of fluid, kg/m^3
σ slip factor
σ_k, σ_ε model constants in Eqs.(A3) and (A4)
τ_w shear stress at a wet wall, Pa
ω impeller rotational speed, r/min
ξ incidence loss in the impeller, see Eq. (7)
∞ impeller at an infinite number of blades

Superscripts

$\bar{\ }$ mean
$\vec{\ }$ vector

Subscripts

1 inlet
2 outlet
a axial direction
c critical
ch pump chamber
fi friction loss in the impeller
fd friction and diffusion loss in the impeller
h hydraulic
i index of number of the points where the fluid velocity profiles are extracted
in incidence loss
m mean
me mechanical
R radial direction
th theoretical
u tangential direction
v volumetric
vb volute body
vn volute nozzle

Abbreviations

1D one-dimensional
2D two-dimensional
3D three-dimensional
BEP best efficiency point
CFD computational fluid dynamics
DEM discrete element method
LDV laser Doppler velocimetry
MRF multiple reference frame
PIV particle image velocimetry
PRESTO pressure staggering option
PS blade pressure side
SIMPLE semi-implicit method for pressure-linked equations

1. Introduction

Vortex pumps are a special kind of rotodynamic pump with a rotating semi-open impeller and casing chamber. The impeller can not only generate a head against the liquid flowing through it, but can also induce a rotating flow in the pump casing chamber. Vortex pumps have found applications in chemical and petrochemical processes, waste-water treatment, and the food and metallurgical industries. Significant studies have been devoted to the hydraulic performance and analysis of the internal fluid flow when a vortex pump works under single-phase, or gas-liquid or solid-liquid two-phase flow conditions.

Studies on the hydraulic performance of vortex pumps have been critical to the design and performance prediction of vortex pumps since the 1960s. For example, the hydraulic performance of a vortex pump was tested under single-phase flow conditions of water to establish a hydraulic design method for the pump when the geometric parameters of the impeller, volute and suction pipe varied [1]. Likewise, the performance of a vortex pump with various geometric parameters, including casing and impeller width, inlet pipe diameter, and casing cross-section shape, was tested and a hydraulic design method was developed in terms of the corresponding experimental data [2]. The effect of the impeller protruding into the pump chamber on the performance of a vortex pump was clarified experimentally, and it was shown that the impeller protruding into the pump chamber could improve the pump head, efficiency and required net positive suction head [3]. The geometric parameters, for example, the impeller diameter, width, blade inlet and outlet angles, volute width, suction pipe diameter, etc., were correlated to the pump head, head coefficient and efficiency at the best efficiency point (BEP) of the vortex pumps found in the literature, and the generated plots are helpful in the hydraulic design of vortex pumps [4]. Under solid-liquid two-phase flow conditions, the hydraulic performance of a vortex pump was tested at different particle sizes and concentrations, and their effects on the pump head and efficiency were obtained, and particle erosion patterns in the impeller hub and blades were observed as well [5]. The hydraulic and suction behaviors of a vortex pump were measured when handling rapeseeds, wheat grains and soya beans at volumetric concentrations up to 6% [6]. It was shown that the two behaviors degraded under those solid-liquid two-phase flow conditions. The clogging behavior of a vortex pump with different impeller designs, e.g., blade outlet angle, number of blades, and impeller diameter, was tested when the pump was handling non-woven textiles in various concentrations; it was demonstrated that a smaller blade angle, a larger number of blades, and a larger impeller diameter were favorable to pumping more textiles, and pumping textiles caused the pump to run at a lower flow rate and poor efficiency, and resulted in increased shaft-power consumption [7].

Measurements of the fluid flow in a vortex pump have become a vital tool to understand the working principle, hydraulic design, and performance prediction of the pump since the 1970s. The air flow in a 1/6-scale model of an Ingersoll-Rand 6×8×18 vortex pump without a volute was measured at various axial and radial positions in the pump chamber by using a calibrated 3-hole cobra probe at four different flow rates. The static pressure on the chamber wall was also measured. Five full-scale vortex pumps with different chamber silhouettes were tested and their hydraulic performance was obtained. The flow rate coefficient at BEP was correlated with the dimensionless chamber's axial width. The head coefficient and shaft-power coefficient of the five pumps were plotted in terms of the flow rate coefficient at BEP, but the efficiency was present against a specific speed and compared with the efficiency of centrifugal pumps. A qualitative model of flow in a vortex pump with radial straight blades, consisting of a through-flow component with a superimposed recirculatory flow between the impeller and the chamber, was put forward. Then, a one-dimensional (1D) analytical theory, in which fluid variables are a function of radius only, was proposed for predicting the performance of the vortex pumps. The analytical theory was composed of four mathematical fluid flow models in four flow regions, i.e., inlet region, recirculatory vortex region in the chamber, impeller region, and volute region. The theory was applied to predict the performance of the 1/6-scale pump under air flow conditions and the five full-scale pumps when handling water. Since the impeller inlet radius and skin friction factor are roughly approximate, the predicted efficiency differed from the experimental efficiency by as much as 10% [8].

The flow patterns on the impeller blades and hub as well as on the casing wall were observed by using the surface oil film technique when a vortex pump was handling water; further, the fluid velocity components were measured at different radial positions and axial positions to the impeller in the pump chamber by employing a five-hole spherical probe. The impeller width and diameter, inlet pipe diameter and chamber width were varied to test their effects on the pump's performance [9]. Based on the oil film patterns observed, the streamlines on the impeller hub were radially outward, the streamlines on the blade surfaces entered the blades at a smaller radius and left at a larger radius. Radially inward streamlines emerged on the chamber walls. The tangential velocity of the fluid rose with the increasing radius up to the impeller tip and declined with the reducing distance to the impeller. The fluid axial velocity on the axial position to the impeller formed an S-shape in the radial direction. The flow model developed in [8] was confirmed. Furthermore, an updated flow model was proposed, where there are five flow regions, i.e., inlet region, recirculatory vortex region in the chamber, two impeller regions, and volute region. The mathematical models for each flow region were derived and applied to predict the pump hydraulic performance and fluid velocities in the pump chamber. Better agreement with the experimental data was achieved in comparison with the analytical theory in [8]. The slip factors were calculated from the measured axial, tangential and radial velocities, and it was shown that the factors remained nearly constant over a range of flow rates [9]. The axial, tangential and radial velocities of water in a standard vortex pump with radial straight blades were measured in four orientations and three axial positions in the pump chamber at different flow rates [10]. The flow model proposed in [8] was verified. The mathematical models for three flow regions, i.e., inlet region, boundary layer on the chamber wall and core flow in the chamber, were developed, and the flow in the meridian plane and tangential velocity were calculated at BEP. The predicted flow velocity and static pressure rise in the chamber agreed well with the experimental data [10]. Based on the experimental method in [10], the velocity and total pressure of water in the pump chambers of 13 vortex pumps with different blade angles, impeller widths, and numbers of blades were measured at four flow rates [11]. The pump efficiency was discomposed into hydraulic efficiency, recirculatory efficiency and mechanical efficiency. The recirculatory efficiency should be referred to as volumetric efficiency. The impeller theoretical heads with infinite and finite numbers of blades were determined with the measured velocity components near the impeller. The effects of those geometric factors on the hydraulic, volumetric, mechanical efficiencies and theoretical head were clarified [11]. Additionally, the reaction degree of the impeller, critical radius for zero axial velocity, and slip factor were deduced from the measured velocities near the impeller, then an empirical method was developed to estimate the hydraulic performance of a vortex pump. The predicted performance curves agreed reasonably well with the tested curves [12]. Interestingly, the static pressure on the impeller blade surfaces of a vortex pump and relative flow velocities were measured by using miniature holes in the blades and a 3-hole Pitot probe when pumping water at three flow rates [13]. Radial profiles of three velocity components and the fluctuation intensity of the water flow in the mid-span of the pump chamber and impeller of a vortex pump were mapped by employing 3D laser Doppler velocimetry (LDV); it turned out that there was preswirl in the impeller inlet [14]. The velocity and pressure of the water were measured with a five-hole spherical probe in the mid-span of the pump chamber in four orientations when a vortex pump was handling water [15]. The flow parameters of an air-water two-phase flow in the pump chamber of a vortex pump were measured by using a Pitot probe [16, 17]. A considerable concentration of air bubbles was found in the recirculatory flow region [16]. Two-dimensional (2D) dilute salt crystal-liquid two-phase flows in the impeller of a vortex pump in [18–20] and in the pump chamber in [20] were measured by making use of particle image velocimetry (PIV). There was a little slip between the two phases and the solid phase mainly accumulated in the chamber and blade pressure sides [20]. However, no new flow models were proposed for vortex pumps based on those advanced measurements so far.

Numerical simulations of 3D flow have played an important role in the understanding of the fluid flow characteristics in the vortex pump since the 1980s but have also served as an effective tool in hydraulic design and optimization of the pump recently. Initially, the fluid flow in the impeller of a vortex pump was calculated numerically based on a quasi-3D potential flow model by using the streamline curvature method [21], then based on a 3D potential flow model and boundary element method [22]. Since the 2000s, numerical simulations of 3D, steady, incompressible, and turbulent flows of water in vortex pumps have become dominant based on commercial computational fluid dynamics (CFD) software and the flow pattern proposed in [8] was confirmed numerically [23–27]. The vortex in the pump chamber is similar to the Hamel-Oseen vortex only at a very low flow rate [28]. Furthermore, two secondary vortices were identified in cross-sections of the volute of a vortex pump [29]. The secondary vortices had little influenced on the efficiency of the pump, but the recirculatory flow reduced the efficiency greatly [30]. The characteristics of hydraulic loss in a vortex pump were analyzed under part-load, design and over-load conditions based on the results of a CFD simulation in terms of entropy generation. It was shown that a total entropy production totalled 70% in the pump chamber [31]. An inducer could improve the suction and hydraulic performances of a vortex pump [32]. Additionally, CFD simulations were applied to the design [33] and optimization [34, 35] of vortex pumps. CFD simulations were conducted on 3D, unsteady, incompressible, and turbulent flows of water in a vortex pump, and the flow pattern in [8] was verified [36].

A couple of CFD simulations of a steady 3D turbulent solid-liquid two-phase flow were carried out and indicated that solid particles could deposit on the blade pressure side and volute [37, 38]. The size of both the recirculatory vortex and secondary vortex depends on the solid particle volumetric concentration [39]. The strength of the recirculatory vortex reduced with the increasing particle volumetric concentration, but the blade shape exhibited a greater influence on the strength than the concentration [40]. String-like material and cloth-like material motions in a vortex pump were simulated by using the discrete element method (DEM) in the STAR-CCM CFD software, and the effect where the strings were pulled back into the pump by the backflow near the tongue of the volute was observed [41]. Unsteady cavitating flows of water in a vortex pump product were simulated with ANSYS CFX with turbulence and cavitation models in [42]. The performance and flow of a vortex pump were predicted with the ANSYS Fluent CFD software at six different viscosities of the fluids [43]. The size of the recirculatory and secondary vortices and through-flow was analyzed based on flow fields of the fluids at three different viscosities simulated by the CFD software, and the size of the recirculatory vortex and though-flow was significantly affected by both the viscosity and flow rate. The size of the secondary vortex, however, was less influenced by them [44].

Quantitative details of the fluid flow in the impeller inlet and outlet of a vortex pump are critical to the hydraulic design of the impeller of a vortex pump. Unfortunately, in the CFD studies mentioned above, these quantitative details in the impeller inlet and outlet have been ignored. The slip factor in the outlet and the incidence loss in the inlet were also not clarified. The profiles of fluid dimensionless velocity components in the inlet and outlet were not analyzed. In the article, as a further study of [43], the axial, radial and tangential velocity components of the fluids were extracted from CFD simulation results at a series of points in the pump chamber with a 1mm distance to the blades. The critical radius was decided based on the axial velocity radial profiles to determine the impeller inlet and outlet at various viscosities and flow rates. A mean-line flow model and hydraulic loss model were built based on those profiles. The incidence loss in the inlet and the slip factor in the outlet was calculated at part-load, design, and over-load points at various viscosities. The impeller theoretical head, hydraulic efficiency and volumetric efficiency were obtained and discussed. The work is undocumented in the literature.

2. Analytical Methods

2.1. Pump specifications

A motor-connected vortex pump of model 32WB8-12 is shown in Fig. 1. The pump specifications and primary geometric dimensions are listed in Table 1. The hydraulic performance of the pump was tested under water single-phase [14], solid-water [6] and air-water [16] two-phase flow conditions, respectively. This pump was employed to identify the influence of the liquid viscosity on its hydraulic performance and fluid flow in [43] and was adopted here once again.

2.3. CFD simulations

The fluid domains, flow models, mesh, boundary conditions and numerical methods are identical to those adopted in [43], which are summarized in Appendix A. The CFD simulations were performed at the flow rates Q = 0, 2, 4, 6, 8, 10, 12.m^3/h and the viscosities and densities listed in Table 2, respectively. Q = 0 m^3/h means that there is no flow into or out of the pump, but there is a flow inside the pump induced by the impeller's rotation. After all the CFD simulations were completed, three velocity components at 16 points 1mm ahead the blade tip were extracted. These velocity components, at one point, represent the circumferentially averaged values on the circle through that point.

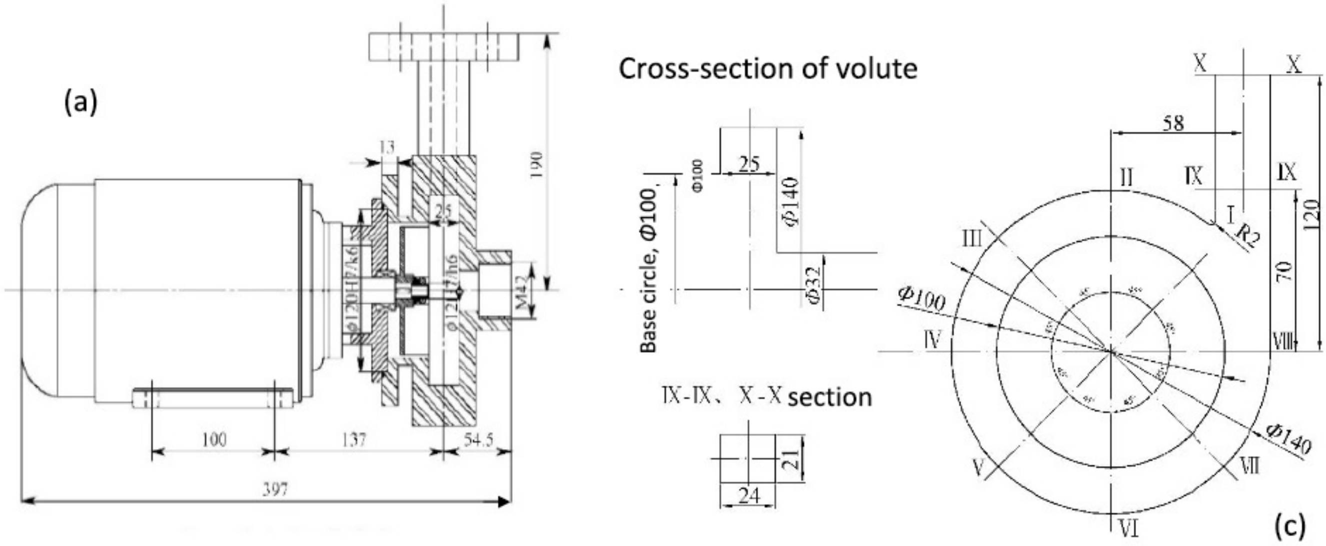

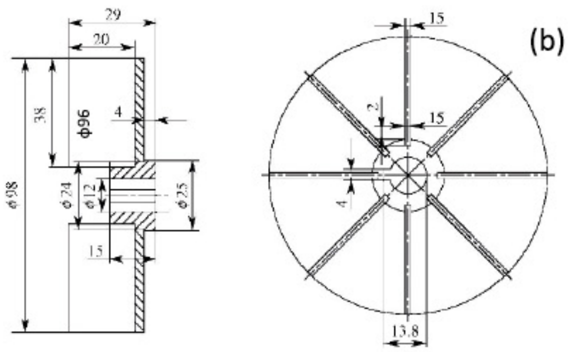

Figure 1. Cross-sectional drawing of the vortex pump (a), drawing of the impeller (b), and volute (c), the pictures were adapted from [6, 14].

2.2. Working fluids

Tap water and machine oils were used as working liquids, their density and kinematic viscosity, and the impeller Reynolds numbers are tabulated in Table 2. These oils are mineral oils, where "Oil 1" to "Oil 5" in the table represent 10#, 22#, 32#, 68# and 100# mineral oil, respectively. The number before the hash is the kinematic viscosity of the mineral oil at 40°C in cSt (1×10^{-6} m^2/s or 1 mm^2/s) based on ISO 3448. These viscous oils with a high viscosity are employed as highly viscous liquids to study the effects of viscosity on the hydraulic performance and flow of the vortex pump.

2.4. Mean-line flow model

The mean-line flow model, i.e., 1D flow model, is commonly applied to design the impeller, volute, and diffuser of a centrifugal pump and to predict the performance of the pump designed. In the flow model, it is assumed that the fluid velocity and pressure vary along the mean-line or flow path, and are uniform in the cross-sections perpendicular to the line. There is an angle of attack or incidence in the impeller inlet, but there is the slip factor or deviation angle in the impeller outlet based on the velocity triangles in the outlet. The total head generated by an impeller yields the Euler's turbomachinery equation [47]. The pump total efficiency can be decomposed into hydraulic efficiency, volumetric efficiency and mechanical efficiency. The hydraulic loss and disc friction loss in the pump can be estimated by using solutions of viscous fluid flow and empirical correlations in fluid mechanics [48].

Table 1. Pump specifications and primary geometric parameters

Classification	Parameter/type	Value/shape
Design condition	Flow rate Q (m^3/h)	8
	Head H (m)	12
	Rotational speed n (r/min)	2850
	Specific speed n_s*	76
Impeller hydraulic dimension	Impeller diameter D_2 (m)	96
	Blade shape	Radial, straight
	Blade width b (mm)	20
	Blade metal thickness δ (mm)	1.5
	Number of blades Z	8
Volute hydraulic dimension	Volute shape	Concentric
	Width b_3 (mm)	25
	Base circle radius R_3 (mm)	50
	Volute radius R_4 (mm)	70
Pump inlet and outlet dimension	Inlet diameter (mm)	32
	Outlet size $b_4 \times a_4$ (mm)	24×21

An axial velocity radial profile near the blade side tip given by the CFD method above is illustrated in Fig. 2(a). In the profile, there is a point where the axial velocity is zero. The radius at zero axial velocity is called critical radius R_c. This definition indicates that a critical radius R_c is decided by the axial velocity radial profile near the blade side tip. The liquid flows into the impeller in the range: $R_1 \le R \le R_c$ through the side tip and flows out of the impeller in the range: $R_c \le R \le R_2$ through that tip. Obviously, those two regions in the blade side tip serve as the impeller inlet and outlet, respectively.

Table 2. Density and kinematic viscosity of tap water and machine oils at 20°C

Liquid	Water	Oil 1	Oil 2	Oil 3	Oil 4	Oil 5
Density (kg/m^3)	1000	839	851	858	861	865
Kinematic viscosity (cSt or m^2/s)	1	24	48	60	90	120
Impeller Reynolds number	6.8763×10^5	2.8651×10^4	1.4326×10^4	1.1461×10^4	7.6404×10^3	5.7303×10^3

To implement the mean-line flow model, a uniform axial velocity profile is assumed each in the inlet and outlet of the impeller, as shown in Fig. 2(b). The uniform axial velocity magnitude is determined by using the identical flow rate through the impeller, i.e. the flow rates from the axial velocity profiles through the inlet and outlet in Fig. 2(a) are the same as the flow rates based on the uniform axial velocity profiles across the inlet and outlet in Fig. 2(b):

$$\begin{cases} Q_{th} = 2\pi\int_{R_1}^{R_c} V_a(R)R\,dR = \pi\overline{V}_{a1}(R_c^2 - R_1^2) \\ Q_{th} = 2\pi\int_{R_c}^{R_2} V_a(R)R\,dR = \pi\overline{V}_{a2}(R_2^2 - R_c^2) \\ Q_{th} = Q + q \end{cases} \tag{1}$$

where Q_{th} is the theoretical flow rate through the impeller, Q is the flow rate through the pump, and q is the flow rate of the recirculatory or leakage flow. Here, Q, V_a (R) and R_c are known, thus Q_{th} and q can be determined.

According to Eq. (1), the two uniform axial velocities are calculated by:

$$\begin{cases} \overline{V}_{a1} = \frac{2\int_{R_1}^{R_c} V_a(R)RdR}{R_c^2 - R_1^2} \\ \overline{V}_{a2} = \frac{2\int_{R_c}^{R_2} V_a(R)RdR}{R_2^2 - R_c^2} \end{cases} \tag{2}$$

Since the axial velocity is uniform in the inlet and outlet of the impeller, the mean effective or mean-line radii at the inlet and outlet of the impeller are determined by the expressions [49]:

$$\begin{cases} R_{1m} = \sqrt{(R_1^2 + R_c^2)/2} \\ R_{2m} = \sqrt{(R_c^2 + R_2^2)/2} \end{cases} \tag{3}$$

The theoretical head produced by the impeller is determined by using the Euler equation for turbomachinery and written as [47, 48]:

$$H_{th} = \frac{1}{g}\left(\overline{V}_{u2}u_2 - \overline{V}_{u1}u_1\right) \tag{4}$$

where H_{th} is the theoretical head, $\overline{V}_{u1}$ and $\overline{V}_{u2}$ are the mean tangential velocities of the fluid at radii R_{1m} and R_{2m}, u_1 and u_2 are the circumferential velocities of the impeller at radii R_{1m} and R_{2m}, and g is the acceleration due to gravity. $\overline{V}_{u1}$ and $\overline{V}_{u2}$ are extracted from the CFD simulation results by the following mass-averaged expressions:

$$\begin{cases} \overline{V}_{u1} = \frac{\int_{R_1}^{R_c} V_a(R)V_u(R)RdR}{\int_{R_1}^{R_c} V_a(R)RdR} \\ \overline{V}_{u2} = \frac{\int_{R_c}^{R_2} V_a(R)V_u(R)RdR}{\int_{R_c}^{R_2} V_a(R)RdR} \end{cases} \tag{5}$$

As indicated in Fig. 2(c), the incidence or angle of attack and incidence loss can be determined based on two velocity triangles at radius R_{1m} in the inlet, one is the triangle with a finite number of blades, and one is the triangle with an infinite number of blades. The incidence and its loss are expressed by:

$$\begin{cases} \Delta\overline{\beta}_1 = \beta_{b1} - \overline{\beta}_1 \\ h = \frac{1}{2g}\Delta\overline{V}_{u1}^2 = \frac{1}{2g}\overline{\xi}u_1^2 \end{cases} \tag{6}$$

where $\Delta\overline{V}_{u1}$ is the incidence, β_{b1} is the blade angle at R_{1m}, β_{b1}=90°, $\overline{\beta}_1$ is the flow angle at R_{1m}, h is the incidence loss, $\Delta\overline{V}_{u1}$ is the incidence velocity loss, $\overline{\xi}$ is the incidence loss coefficient, u_1 is the blade speed at R_{1m}, $u_1 = \omega R_{1m}$, ω is the angular speed of the impeller, and $\overline{\beta}_1$, $\Delta\overline{V}_{u1}$ and $\overline{\xi}$ are determined by the CFD simulation results, and yield the following expressions:

$$\begin{cases} \Delta\overline{V}_{u1} = u_1 - \overline{V}_{u1}, \overline{\beta}_1 = \pi/2 - tan^{-1}(\Delta\overline{V}_{u1}/\Delta\overline{V}_{a1}), \Delta\overline{\beta}_1 \ge 0 \\ \Delta\overline{V}_{u1} = \overline{V}_{u1} - u_1, \overline{\beta}_1 = \pi - tan^{-1}(\Delta\overline{V}_{u1}/\Delta\overline{V}_{a1}), \Delta\overline{\beta}_1 < 0 \\ \overline{\xi} = (\overline{V}_{u1}/u_1)^2 \end{cases} \tag{7}$$

As shown in Fig. 2(d), the slip velocity and slip factor or deviation angle occur at radius R_{2m} in the outlet in terms of two velocity triangles, i.e., the triangle with a finite number of blades and the triangle with an infinite number of blades. The slip velocity and slip factor are calculated by the following expressions:

$$\begin{cases} \Delta\overline{V}_{u2} = u_2 - \overline{V}_{u2} \\ \overline{\sigma} = \Delta\overline{V}_{u2}/u_2 = 1 - \overline{V}_{u2}/u_2 \\ \Delta\overline{\beta}_2 = \beta_{b2} - \overline{\beta}_2 \end{cases} \tag{8}$$

where $\Delta\overline{V}_{u2}$ is the mean velocity slip, $\overline{V}_{u2}$ is the mean tangential velocity of the fluid, u_2 is the blade speed at R_{2m}, $u_2=\omega R_{2m}$, and$\Delta\overline{\beta}_2$ is the deviation angle.

Based on a V_a radial profile predicted via CFD simulations, the impeller theoretical flow rate and the corresponding pump volumetric efficiency can be calculated with the following expressions:

$$Q_{th} = 2\pi \int_{R_c}^{R_2} V_a(R)R\,dR,\ \eta_v = \frac{Q}{Q_{th}} \tag{9}$$

where η_v is the pump volumetric efficiency.

At each point in the axial, radial and tangential velocity profiles, there are velocity triangles like those shown in Fig. 2. Based on these triangles, the local inflow angle β_1, incidence $\Delta\beta_1$, incidence loss coefficient ξ in the inlet, outflow angle β_2, deviation angle$\Delta\beta_2$ and slip factor σ in the outlet can be obtained.

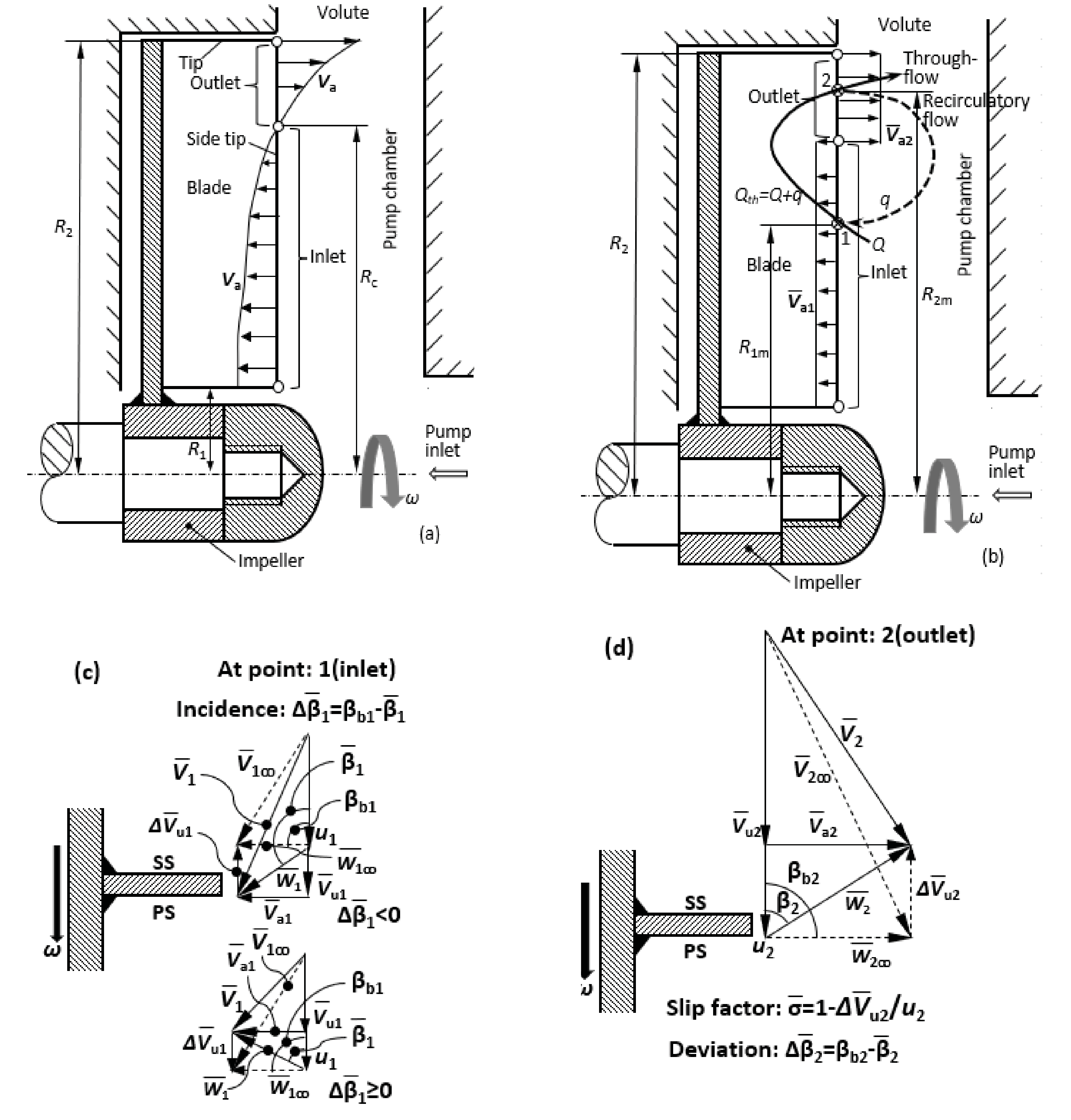

Figure 2. Axial velocity radial profile near the blade side tip and critical radius (a), simplified axial velocity profile, inlet and outlet (b), inlet velocity triangles, incidence/angle of attack (c), outlet velocity triangles (d)

3. Results

3.1. Fluid velocity radial profiles

The dimensionless axial, radial and tangential velocities of the fluids at various flow rates and viscosities are illustrated in Figs. 3, 4 and 5, respectively. These dimensionless velocities at R are the actual velocities normalized by using the blade speed at that R, and expressed as:

$$v_a = V_a/u,\ v_R = V_R/u,\ v_u = V_u/u,\ u = R\omega,\ r = R/R_2 \quad (10)$$

where v_a, v_R and v_u are the dimensionless axial, radial and tangential velocities of the fluids at R, V_a, V_R and V_u are the corresponding actual axial, radial and tangential velocities, u is the blade speed at that R, and r is the dimensionless radius.

a given viscosity, and the smaller the viscosity, the wider the region at a fixed flow rate.

In Fig. 5, v_u<1 means the tangential velocity of the fluids is slower than the blade speed, v_u=1 means the tangential velocity is equal to the blade speed, while v_u>1 means the tangential velocity of the fluids is faster than the blade speed. At Q≥12m^3/h, the velocity v_u increases steadily until r=0.88, then declines toward r=1 due to the slip effect. At the other flow rates, however, the maximal velocity v_u appears in a region of the inlet where v_R<0 or v_a≈0 applies. In particular, v_u>1 can be seen in that region, indicating a faster tangential velocity of the fluids than the blade speed. The lower the flow rate, the wider the region with v_u>1.

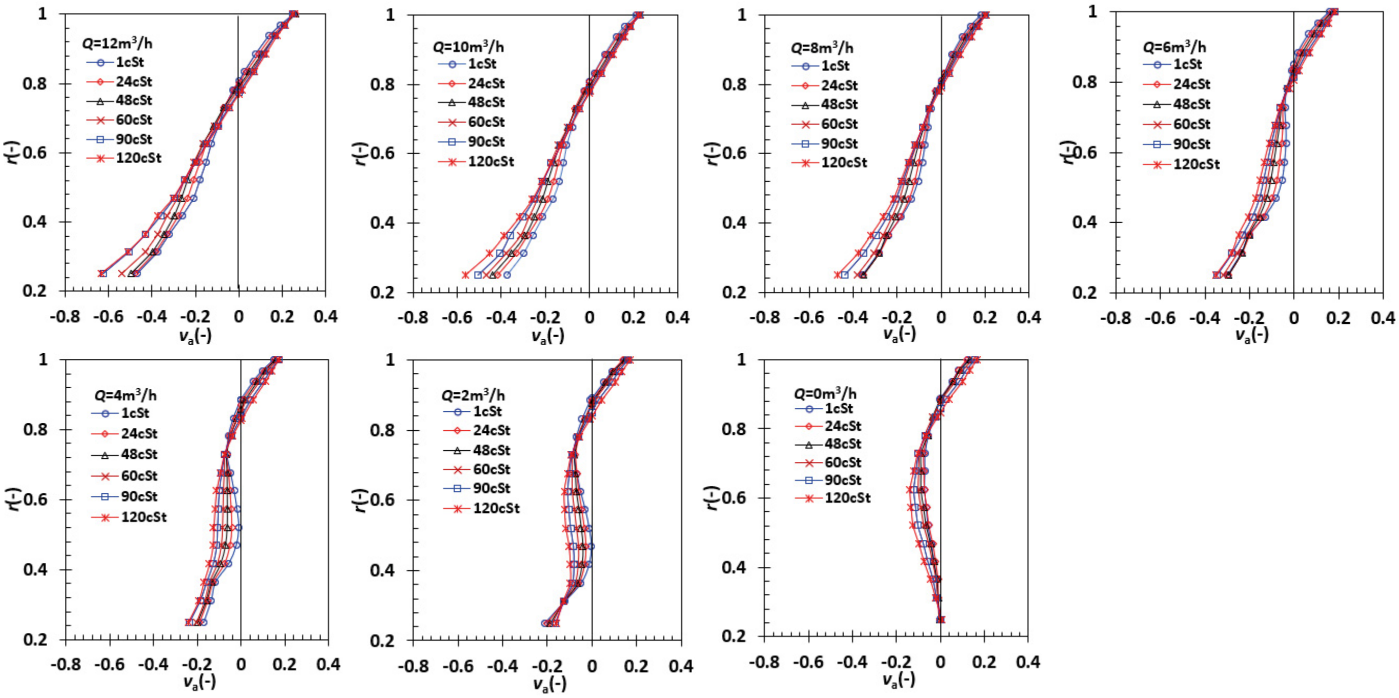

Figure 3. Dimensionless axial velocity v_a in the radial direction R at Q=0, 2, 4, 6, 8, 10, 12 m^3/h, ν=1, 24, 48, 60, 90, 120 cSt

In Fig. 3, the region v_a<0 means a fluid enters the impeller through the inlet, while the region v_a>0 indicates the fluid leaves the impeller through the outlet. The v_a=0 point defines the boundary between the inlet and the outlet, and the corresponding radius is called the critical radius here. The v_a profiles are closely linked to the pump flow rate, i.e., the higher the flow rate, the larger the velocity magnitude, and the steeper the velocity gradient with respect to the radius, especially in the inlet. There is a zone with near zero velocity in the inlet at a few viscosities as the flow rate is equal to or less than 4 m^3/h. This means that the axial flow is stalled partially in the inlet as Q≤4 m^3/h. The axial flow of the fluid with a lower viscosity is more likely partially stalled in the inlet.

In Fig. 4, v_R>0 means that the flow is outward but v_R<0 suggests that the flow is inward. The v_R profiles are greatly affected by the flow rate. As the flow rate is at 12 m^3/h, v_R>0 is held and the radial flow is outward; otherwise, a region with v_R<0 exists, and an inward flow emerges in the inlet. The size of the region relies on the flow rate and the viscosity in the inlet, i.e., the lower the flow rate, the wider the region at

3.2. Dimensionless critical radius

Based on the v_a radial profiles shown in Fig. 3, the critical radius R_c can be determined with the v_a=0 condition, and the dimensionless critical radius r_c(=R_c/R_2) is illustrated in Fig. 6 as a function of the flow rate at six viscosities or as a function of the viscosity at seven flow rates. The radius is determined by using the condition where the axial velocity profiles predicted by CFD are zero. Basically, r_c is ranged in 0.77–0.89 but depends on both the flow rate and viscosity. At a given fluid viscosity, r_c reduces with the increasing flow rate. At a fixed flow rate, the radius declines with the increasing viscosity, especially at a viscosity higher than 48 cSt.

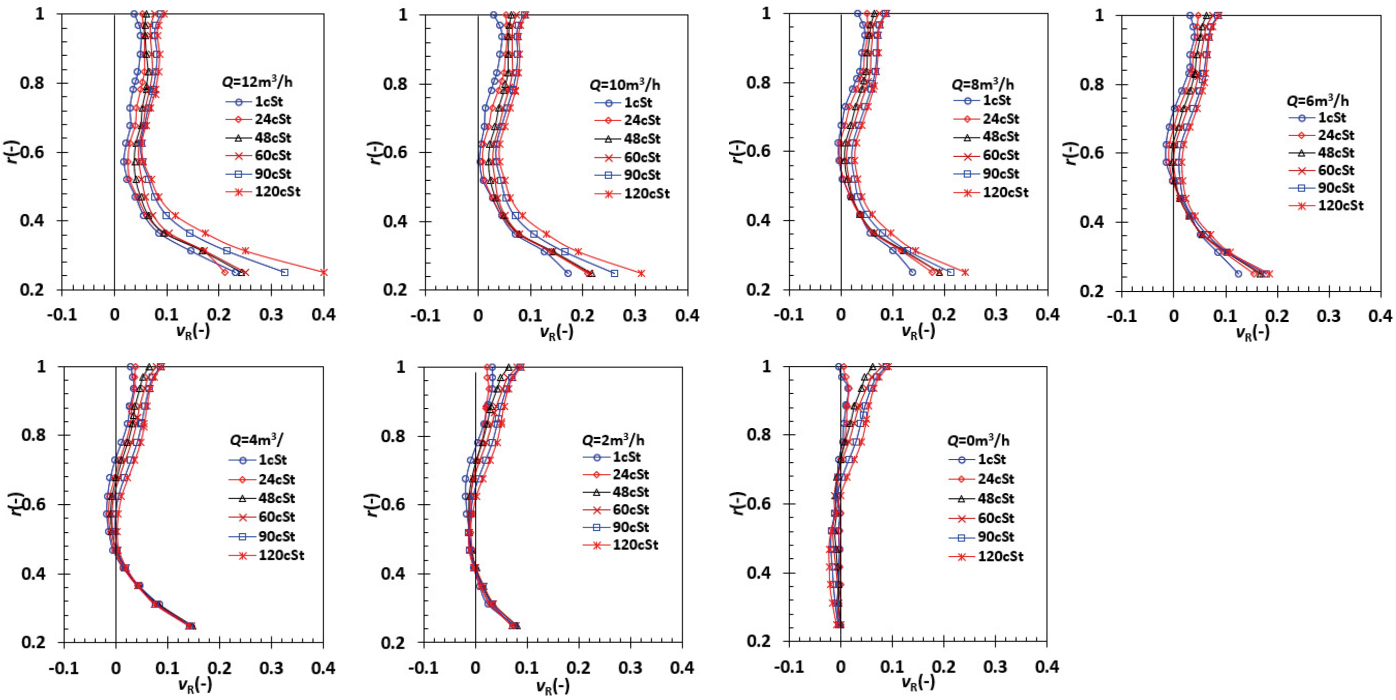

Figure 4. Dimensionless radial velocity v_R in the radial direction R at Q=0, 2, 4, 6, 8, 10, 12 m^3/h, ν=1, 24, 48, 60, 90, 120 cSt

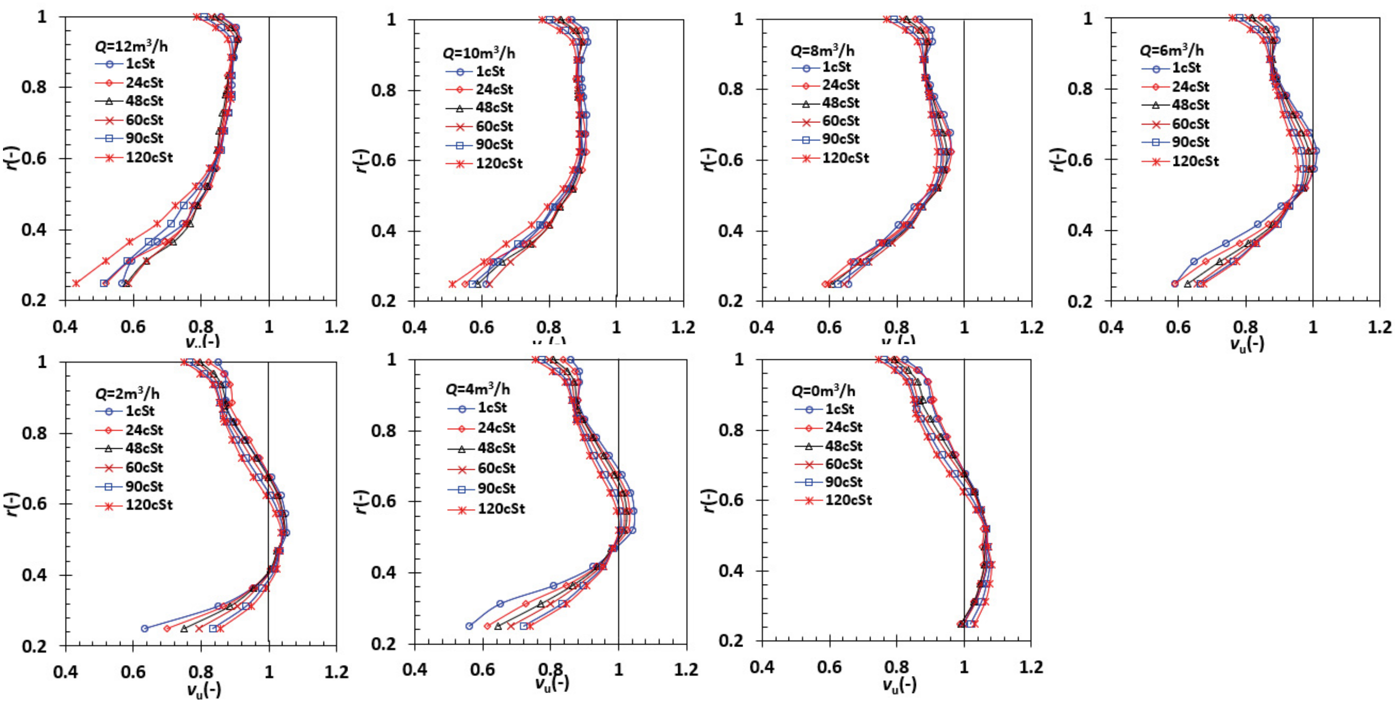

Figure 5. Dimensionless tangential velocity v_u in the radial direction R at Q=0, 2, 4, 6, 8, 10, 12 m^3/h, ν=1, 24, 48, 60, 90, 120 cSt

3.3. Incidence and deviation angle

There is a series of velocity triangles like those shown in Fig. 2(d) at each point in the inlet and outlet of the impeller. Accordingly, there is a series of incidence profiles and a series of deviation angle profiles in the radial direction. These profiles at seven flow rates and six viscosities are illustrated in Fig. 7. The profiles of incidence $\Delta\beta_1$ and deviation angle $\Delta\beta_2$ at one flow rate are similar to the profiles at Q=12, 10 m^3/h (over-load points). As a matter of fact, the incidence $\Delta\beta_1$ remains unchanged in the region: 0.25≤r≤0.6, then rises to 90° until r_c. The deviation angle $\Delta\beta_2$ starts to decline quickly from r_c at 90° to r≈0.7 at about 30–40°, then slightly increases toward r=1. At Q=8 m^3/h (design point), the incidence $\Delta\beta_1$ reduces from r=0.25 to r=0.6, then rises from there to r_c. The deviation angle $\Delta\beta_2$ profile resembles the profiles at Q=12, 10 m^3/h. At Q≤6 m^3/h (part-load point), the incidence $\Delta\beta_1$ declines so much that the $\Delta\beta_1$<0 situation occurs in a region between r=0.25 and r_c, depending on both the viscosity and especially the flow rate. The higher the flow rate, the bigger the range with $\Delta\beta_1$<0 at a fixed viscosity; alternatively, the lower the viscosity, the wider the range with $\Delta\beta_1$<0 at a fixed flow rate. The deviation angle $\Delta\beta_2$ reduces quickly in the radial direction when the flow rate is lowered.

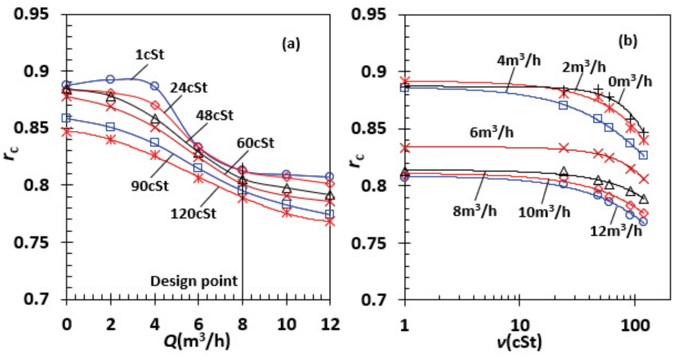

Figure 6. Dimensionless critical radius r_c (=R_c/R_2) is plotted as a function of flow rate at six viscosities (a), or as a function of viscosity at seven flow rates (b), the radius is determined by using the predicted axial velocity profiles

3.4. Incidence loss coefficient and slip factor

The incidence loss coefficient ξ and slip factor σ profiles in the radial direction are shown in Fig. 8 at seven flow rates and six viscosities. The two parameters vary greatly in the radial direction, and their profiles relate to the flow rate closely. Interestingly, the maximum ξ finds itself at r=0.25 at any flow rate. The minimum ξ, however, is located at r_c at Q=10, 12 m^3/h, and in the range around r=0.6 at the other flow rates. The v_u radial profiles shown in Fig. 5 are responsible for the ξ radial variations. The slip factor σ increases from r_c to r_2, and the higher the viscosity, the larger the slip factor.

The radially averaged incidence loss coefficient $\overline{\xi}$ and slip factor $\overline{\sigma}$ are plotted as a function of the flow rate at six viscosities in Fig. 9. $\overline{\xi}$ rises with increasing flow rate, especially at a higher viscosity. $\overline{\sigma}$ declines with the increasing flow rate, particularly for the fluids with a higher viscosity.

3.5. Theoretical head and pump head

The theoretical head H_{th} expressed by Eq. (4) was calculated and plotted as a function of the flow rate Q at six viscosities in Fig. 10(a), where the experimental data at ν=1cSt in [14] are included and compared. H_{th} rises with the increasing Q at six viscosities but is below the experimental data. This phenomenon does not make sense because the impeller should theoretically be above the experimental data at the same viscosity. The lowered H_{th} is attributed to the pre-swirl of fluid caused by the impeller.

If we let $\overline{V}_{u1}$=0, then H_{th} is recalculated and replotted in Fig. 10(b). All the H_{th} curves are higher than the experimental data. The shape of the H_{th} curves resembles the shape of the experimental head curve, too. Based on the velocity profile predicted by CFD simulation, pre-swirl in the inlet of pump chamber doesn't exist, V_{u1}=0 means that the H_{th} of a vortex pump represents the total head from the inlet of the pump chamber to the impeller outlet rather than from the impeller inlet to the impeller outlet as in a centrifugal pump. Essentially, the pump chamber is a container for accommodating the liquid energized by the impeller in a vortex pump.

The hydraulic losses in the impeller, chamber and volute were estimated based on a 1D hydraulic loss, respectively. Then the pump head was calculated by subtracting these losses from the theoretical head shown in Fig. 10(b). The estimated head-flow rate curves at six viscosities are illustrated in Fig. 10(c). The 1D hydraulic loss model is summarized in Appendix B.

In Fig. 10(c), the pump head-flow rate curves predicted by the CFD simulations in [43] are included, too. The head-flow rate curves estimated by using the 1D hydraulic model are comparable to the curves predicted based on the CFD simulations. This fact indicates that the impeller theoretical head-flow rate curves shown in Fig. 10(b) are reasonable. If the theoretical head-flow rate curves shown in Fig. 10(a) are adopted, the pump head-flow rate curves predicted with the 1D hydraulic loss model will be much smaller than those predicted by using the theoretical head-flow rate curves.

In Fig. 10(d), the dimensionless mean tangential velocities in the inlet and outlet – $\overline{V}_{u1}/\omega R_{1m}$, $\overline{V}_{u2}/\omega R_{2m}$ – are illustrated. The $\overline{V}_{u1}/\omega R_{1m}$ profiles are affected more greatly by the flow rate than by the viscosity, in particular, it increases with the decreasing flow rate. This trend agrees well with the trend of v_u in the region r<r_c shown in Fig. 5. $\overline{V}_{u2}/\omega R_{2m}$ increases with the increasing flow rate but decreases with the increasing viscosity. $\overline{V}_{u2}/\omega R_{2m}$ is more strongly influenced by the viscosity than by the flow rate. The feature in the profiles of $\overline{V}_{u1}/\omega R_{1m}$ versus the flow rate is responsible for the shape of the theoretical head-flow rate curves in Fig. 10(c).

3.6. Volumetric efficiency and hydraulic efficiency

The volumetric efficiency η_v estimated by Eq. (9) and the hydraulic efficiency η_h calculated with Eq. (B11) are illustrated in Fig. 11. The hydraulic and volumetric efficiencies predicted by CFD simulations in [43] are presented in the figure, too. The η_v and η_h curves given by Eq. (9) and Eq. (B11) are similar in shape to the curves provided by the CFD simulations, but the values of the former are higher than the latter by around 0.2 in η_v at ν=1cSt and Q=12 m^3/h, and about 0.12 in η_h at ν=1 cSt and Q=0 m^3/h.

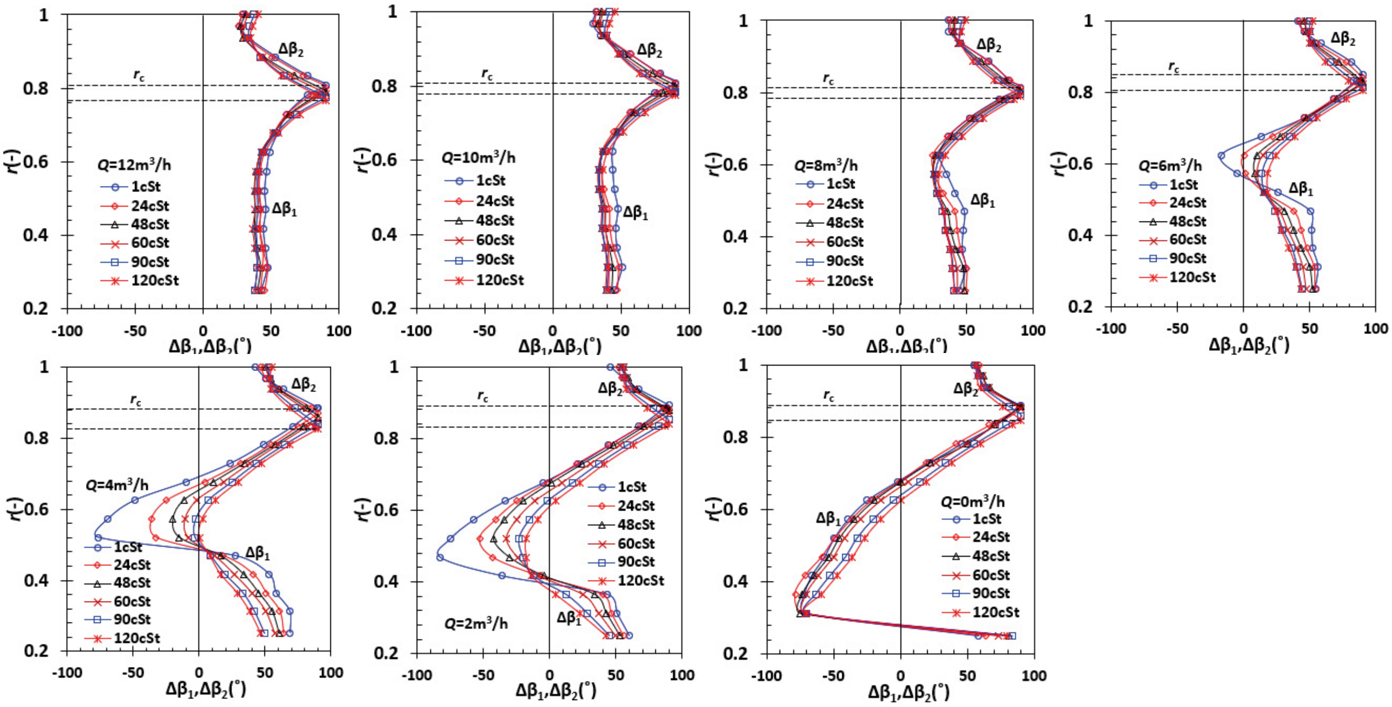

Figure 7. Incidence/angle of attack along the radius at Q=0, 2, 4, 6, 8, 10, 12 m3/h, ν=1, 24, 48, 60, 90, 120 cSt

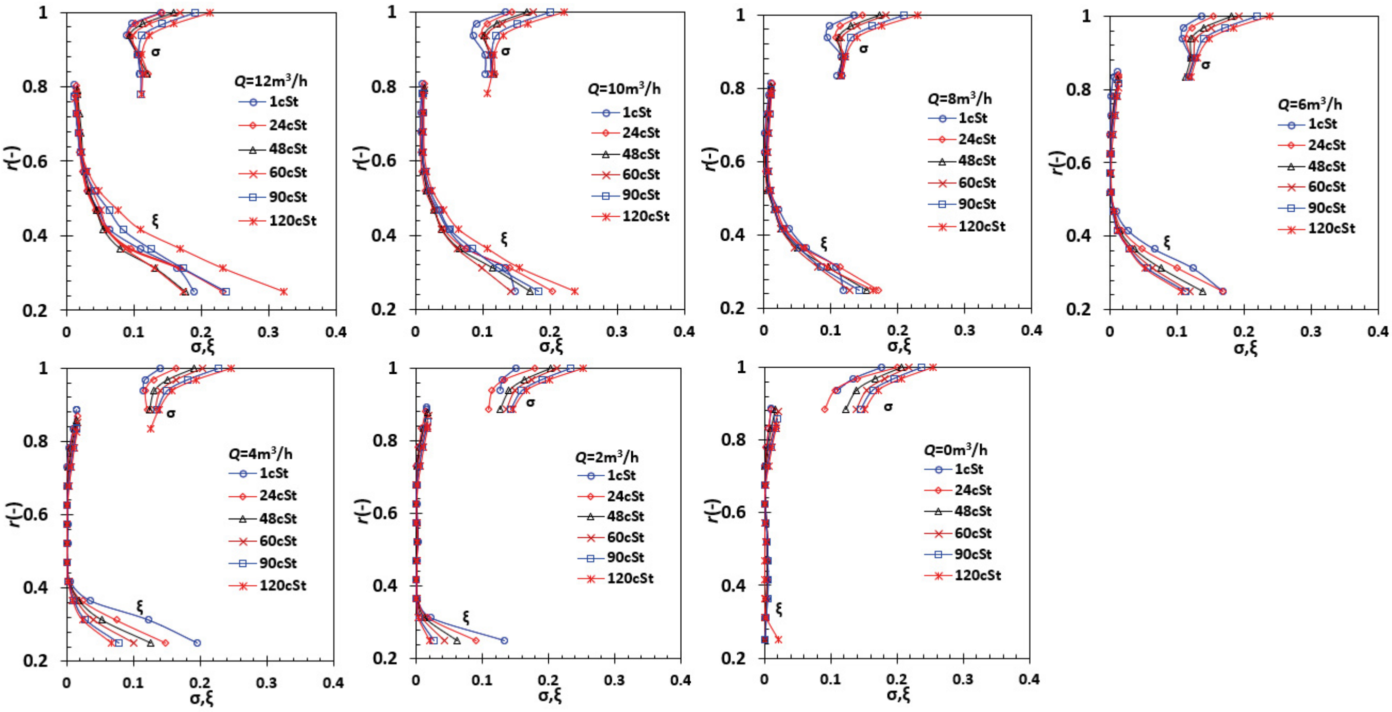

Figure 8. Incidence loss coefficient ξ and slip factor σ along the radius at Q=0, 2, 4, 6, 8, 10, 12 m^3/h, ν=1, 24, 48, 60, 90, 120 cSt

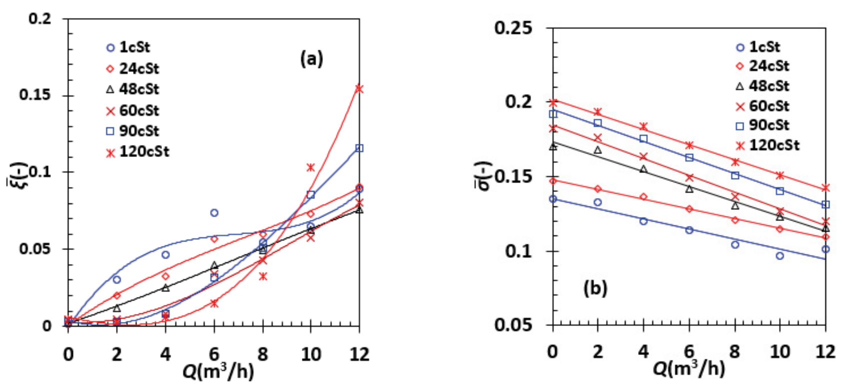

Figure 9. Mean incidence loss coefficient $\bar{\xi}$ and mean slip factor $\bar{\sigma}$ along the radius at Q=0, 2, 4, 6, 8, 10, 12 m^3/h, ν=1, 24, 48, 60, 90, 120 cSt

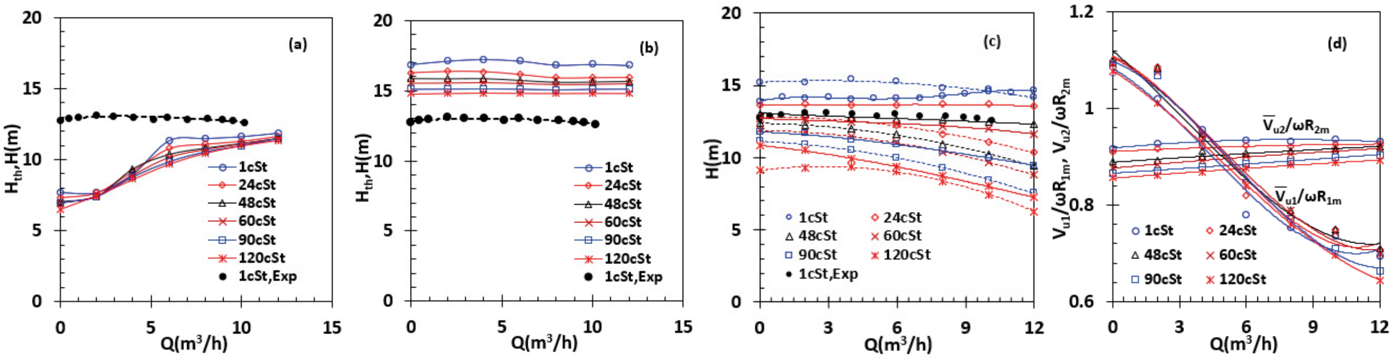

Figure 10. Theoretical head, head, and dimensionless mean tangential velocity flow rate curves, (a) theoretical head between the inlet and outlet of the impeller, (b) theoretical head between the outlet of the impeller and the inlet of the pump chamber, (c) head-flow rate curves, (d) dimensionless mean tangential velocity in the inlet and outlet, solid line – CFD prediction, dashed line – 1D hydraulic loss model, experimental data from [14]

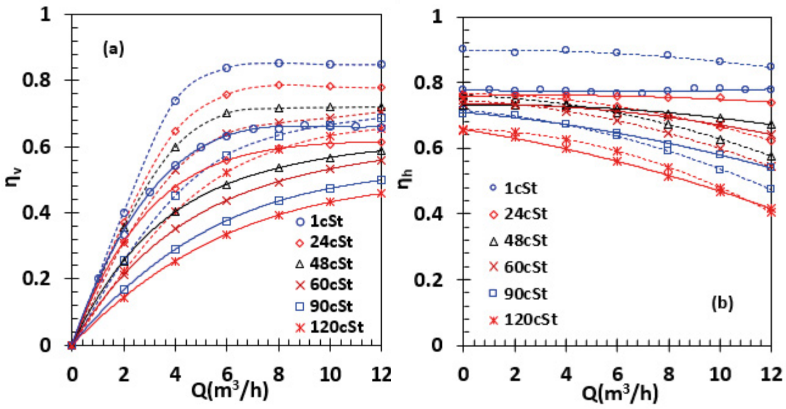

Figure 11. Volumetric efficiency η_v and hydraulic efficiency η_h curves predicted with CFD simulations and 1D hydraulic loss model at six viscosities, (a) η_v, (b) η_h, solid line – CFD prediction, dashed line – 1D hydraulic loss model

The difference in the approach for calculating η_v may be responsible for this phenomenon. Based on the CFD simulations in [43], first, the pump efficiency η was calculated by using the power obtained by the fluids in the pump and the power applied to the impeller; second, the mechanical efficiency η_{me} was calculated by using the power applied to the impeller and the disk friction loss power extracted; third, the fluid mean tangential velocity at R_2 was extracted, the impeller theoretical head was computed with this velocity and the impeller speed at R_2, and η_h was determined with the pump head and impeller theoretical head. Finally, η_v was calculated with η, η_{me} and η_h in terms of the relationship: $\eta=\eta_v\,\eta_h\,\eta_{me}$. In the mean-line flow model, however, η_v is related to the pump flow rate Q and V_a (R) profile only as expressed by Eq. (9).

The hydraulic losses in the impeller, volute and chamber are shown in Fig. 12 as a function of the flow rate. The hydraulic loss in the chamber h_{ch} is the largest but also varies little with the flow rate, followed by the loss in the volute $h_{vb} + h_{vn}$, but the loss in the impeller $h_{fd} + h$ is minor. Note that the hydraulic loss in the chamber is quite small at ν=1cSt compared with the losses at the other viscosities. This hydraulic loss should be responsible for the greatest error in the hydraulic efficiency at ν=1 cSt demonstrated in Fig. 11(b).

4. Discussion

The fluid axial, radial and tangential velocity radial profiles were extracted from the result files of CFD simulations at seven flow rates and six viscosities. A mean-line flow model was built in terms of the critical radius, incidence, deviation angle, slip factor, incidence loss coefficient, theoretical head, 1D hydraulic loss model, volumetric efficiency, and hydraulic efficiency. Such a study is undocumented in the literature so far.

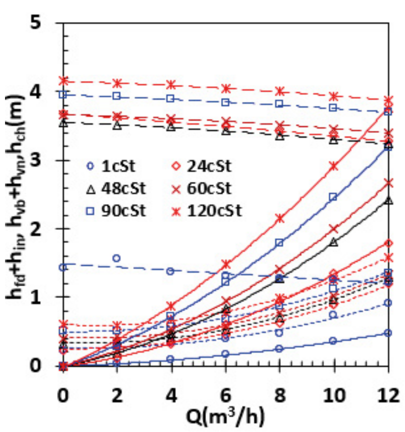

Figure 12. Hydraulic loss curves against flow rate of vortex pump at various viscosities, the hydraulic losses were predicted with the formulas in Appendix B, solid line – hydraulic loss in the volute $h_{vb} + h_{vn}$, short dashed line – hydraulic loss in the impeller $h_{fd} + h$, long dashed line – hydraulic loss in the chamber h_{ch}

Radial straight blades are very commonly employed in the impellers of vortex pumps. A variety of other types of blades can be found in [52]. For vortex pumps with a geometrically similar impeller as the radial straight blade impeller studied here, the mean-line flow model can be employed to estimate their performance. First, the impeller side tip is divided into the inlet and outlet by the critical radius shown in Fig. 6. Second, the theoretical flow rate is determined by using the volumetric efficiency curves in Fig. 11. Third, the mean tangential velocity in the impeller outlet is calculated by using the velocity triangle at an infinite number of blades and the mean slip factor in Fig. 9, as well as the hydraulic loss model in Appendix B.

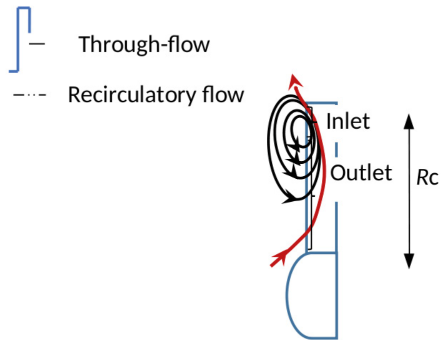

Figure 13. Recirculatory or leakage flow induced by the impeller in a vortex pump

The theoretical head between the outlet and the inlet of the impeller is compared with the theoretical head between the outlet of the impeller and the inlet of the pump chamber at six viscosities in Section 3.5. If the theoretical head is calculated by using the fluid tangential velocity between the outlet and the inlet of the impeller as done for a centrifugal pump, the theoretical head will be quite lower than the experimental head, suggesting an invalid theoretical head. If the theoretical head is estimated by using the fluid tangential velocity between the outlet of the impeller and the inlet of the chamber, the theoretical head will be above the experimental head. The pump head obtained with this theoretical head and the 1D hydraulic loss is comparable to the pump head given by the CFD simulation. Clearly, the theoretical head estimated by using the fluid tangential velocity between the outlet of the impeller and the inlet of the chamber is reasonable. Since the impeller of the vortex pump is semi-open, a swirling flow in the same rotating direction as the impeller is induced by the impeller in the pump chamber. The swirling flow is intensified by the recirculatory or leakage flow (Fig. 13) under part-load flow conditions.

The pump chamber seems to favor and maintain the development of a swirling flow in a vortex pump. There are a few ways to enhance the swirling flow in the chamber, such as: (1) the blade projecting into the chamber [53], (2) the impeller moving into the chamber [54–56], (3) installing a winglet on the blade suction side [33, 57, 58], (4) the combination of (2) and (3) [59, 60], (5) the combination of (2) and blades with different heights [61]. The fluid flow details in the inlet and outlet of the impeller updated in those ways need to be clarified in the future.

Honestly, the article is subject to four drawbacks. First, although the axial, radial and tangential velocity profiles presented here are qualitatively simar to those in [8–10], they should be validated by fresh experimental data in the future. Second, a 1D hydraulic loss model was established but the vortex or separation loss in the impeller was ignored; additionally, the frictional and diffusion losses in the impeller are calculated based on the empirical formulas of 2D straight diffusers, the frictional loss and secondary flow loss in the volute are computed by the empirical correlations of bends, while the friction loss in the chamber is estimated by using empirical correlations of pipes. Those empirical correlations cannot fully cope with the hydraulic losses in the impeller, volute and chamber, since the flow patterns in them are so complicated. As a result, the pump performance predicted by the 1D hydraulic loss model should be different from that given by 3D CFD simulation. Nevertheless, the 1D hydraulic loss model presented here should be validated with more experimental data and updated in the future. Third, the coefficient of 0.75 in Eq. (B4) is used to calculate the mean tangential velocity over the wall of the chamber from the tangential velocity near the blade side tip. It is purely an empirical coefficient and needs to be validated in the future. And finally, the flow models adopted here are steady, and the rotor-stator interaction is handled with MRF systems, so whether the transient effect can influence the mean-line flow model needs to be investigated in the future.

5. Conclusion

Based on the CFD simulation results in [43], the axial, radial and tangential velocity radial profiles at the over-load, design, and part-load points and six viscosities of the fluids were extracted. A mean-line flow model was established according to the profiles. The velocity profiles, critical radius, incidence, deviation angle, incidence loss, slip factor and impeller theoretical head and a 1D hydraulic loss model were presented and discussed. It was found that the axial, radial and tangential velocity radial profiles in the inlet and outlet of the impeller largely depend on the flow rate and viscosity, especially at a low flow rate and in the inlet. A low flow rate and low viscosity result in near zero axial and radial velocities, a faster tangential velocity than the blade speed, negative incidence, and a lower incidence loss coefficient in the inlet. The critical radius decreases with the increasing flow rate and viscosity. The mean slip factor rises with the increasing flow rate and viscosity. The mean incidence loss coefficient grows with the increasing flow rate but increases with the decreasing viscosity under part-load conditions. The dimensionless mean tangential velocity in the inlet rises with the decreasing flow rate, while the dimensionless mean tangential velocity in the outlet decreases with the decreasing flow rate and increasing viscosity. The theoretical head estimated by using the fluid tangential velocity between the outlet of the impeller and the inlet of the chamber is more reasonable than the theoretical head calculated by using the fluid tangential velocity between the outlet and the inlet of the impeller as done in centrifugal pumps. Experimental validation of the velocity profiles and the fluid flow details in the inlet and outlet of the impeller updated with the methods for enhancing the swirling flow in the pump chamber need to be investigated in the future.

Acknowledgment

The work received no external funding and the author declares that there is no conflict of interest.

Appendix A. Mesh, flow models and methodology

Based on the construction of the vortex pump illustrated in Fig. 1, four fluid domains are generated and presented in Fig. A1(a), and a hybrid mesh generated in the domain with mean y^+ at the walls of the suction pipe, impeller and volute for mesh2 at BEP and six viscosities are listed Table A2.

The liquid through the vortex pump is incompressible, and the fluid flow is three-dimensional, steady, and turbulent at any flow rate and viscosity. The governing equations of flow are the Reynolds time-averaged Navier-Stokes equations in

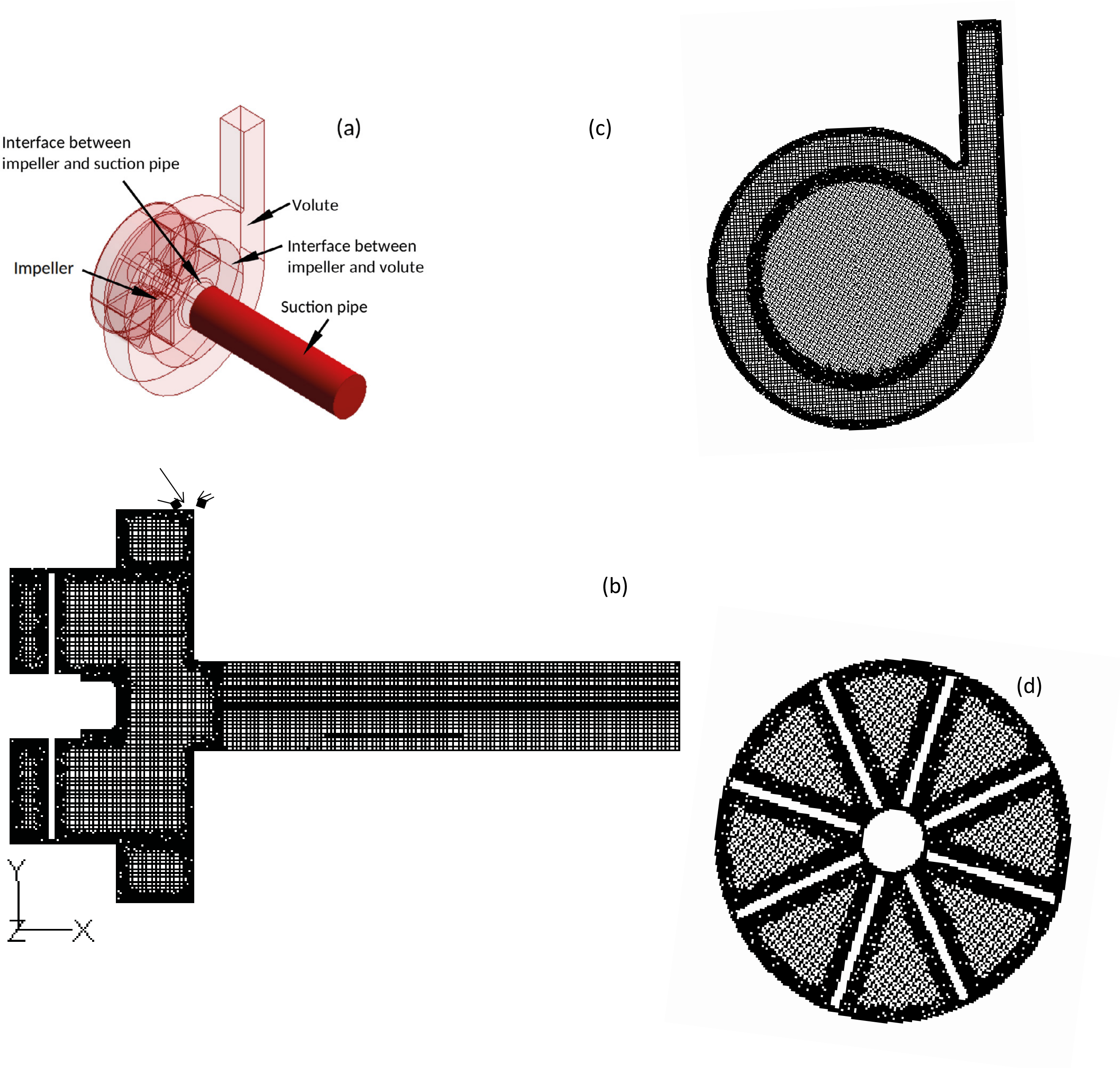

Figure A1. Three fluid domains of the vortex pump (a), mesh structure in pump cross-section (b), in the mid-span of casing chamber (c), in the mid-span of impeller (d)

Gambit is demonstrated in Fig. A1(b)–(d). In the suction pipe fluid domain, the mesh cells are hexahedral. In the impeller and volute fluid domains, the mesh is hybrid, i.e., tetrahedral cells were generated adjacent walls and interfaces, but cubic cells were created in the core fluid regions which are away from the walls and interfaces. The three hybrid meshes shown in Table A1 were created in Gambit to check the effects of the number of mesh elements or cells on the performance curves of the pump. The dependence of the mesh size and the effects of the turbulence model on the pump performance were clarified in [43]. mesh2 was used in all CFD simulations here. The a multiple reference frame (MRF) system. In the MRF system, the continuity equation of flow reads as [45]:

$$\nabla \cdot \left[\rho\left(\vec{V} - \vec{\omega} \times \vec{R}\right)\right] = 0 \tag{A1}$$

and the momentum equations of flow are expressed by [45]:

$$\begin{aligned} \nabla \cdot \left[\rho(\vec{V} - \vec{\omega} \times \vec{R})\vec{V}\right] + \rho\left[\vec{\omega} \times (\vec{V} - \vec{\omega} \times \vec{R})\right] = \\ = -\nabla p + \nabla \cdot \left[(\mu + \mu_t)(\nabla\vec{V} + \nabla\vec{V}^T)\right] \end{aligned} \tag{A2}$$

where $\vec{\omega} = \vec{e}_x \omega$ in the impeller, but $\vec{\omega} = 0$ in a stationary component, $\vec{e}_x$ is the unit vector of the x-coordinate which is along the pump shaft axis, $\vec{R}$ is the coordinate vector of fluid particle, and $\vec{V}$ is the fluid velocity.

The standard $k-\varepsilon$ two-equation turbulence model is applied to estimate the turbulence eddy viscosity, μ_t here. The k and ε equations of the liquid are written as [45]:

$$\nabla\cdot\left(\rho\vec{V}k\right)=\left[\left(\mu+\frac{\mu_t}{\sigma_k}\right)\nabla k\right]+G_k-\rho\varepsilon \tag{A3}$$

and

$$\nabla\cdot\left(\rho\vec{V}\varepsilon\right)=\left[\left(\mu+\frac{\mu_t}{\sigma_\eta}\right)\nabla\varepsilon\right]+\frac{\varepsilon}{k}\left(C_{1\varepsilon}G_k-C_{2\varepsilon}\rho\varepsilon\right)\ \text{(A4)} \tag{A4}$$

where the turbulence eddy viscosity is expressed as $\mu_t=\rho C_\mu k^2/\varepsilon$, $C_\mu=0.09$, the production of turbulence kinetic energy, G_k, is computed by $G_k=\mu_t\left(\nabla\vec{V}+\left(\nabla\vec{V}\right)^T\right):\nabla\vec{V}$; the model constants $C_{1\varepsilon}$, $C_{2\varepsilon}$, C_μ, σ_k and σ_ε take their default values, namely 1.44, 1.92, 0.09,1.0 and 1.3, respectively [45].

Table A1. Mesh and number of mesh cells/elements

Fluid domain	Suction pipe	Impeller	Volute
Type of mesh	Hexahedral	Hybrid	Hybrid
mesh1	26,574	419,209	310,298
mesh2	43,430	543,355	406,303
mesh3	80,520	653,775	581,016

The non-equilibrium wall function was adopted to calculate the wall shear stress. The wall function accounts for the effect of the pressure gradient in the primary flow direction on the stress. The wall function is given by [45]:

$$\left\{V-\frac{1}{2}\frac{dp}{dL}\left[\frac{y_b}{\rho\kappa k^{1/2}}ln\left(\frac{y}{y_b}\right)+\frac{y-y_b}{\rho\kappa k^{1/2}}+\frac{y_b^2}{\mu}\right]\right\}\frac{C_\mu^{1/4}k^{1/2}}{\tau_w/\rho}= \\ =\frac{1}{\kappa}ln\left(E\frac{\rho C_\mu^{1/4}k^{1/2}y}{\mu}\right) \tag{A5}$$

where V is the fluid velocity in the primary flow direction, E is the turbulence constant, y_b is the physical viscous sub-layer thickness, dp/ds is the pressure gradient in the primary flow direction s, κ is Von Karman constant, and τ_w is the wall shear stress.

Table A2. Mean y^+ at the walls of the suction pipe, impeller and volute for mesh2 at BEP and six viscosities

(cSt)	Mean at wall of suction pipe	Mean at wall of impeller	Mean at wall of volute
1	427(265–655)	96.8(3.17–371)	167(8.14–381)
24	25.1(15.6–37.8)	7.22(0.979–29.0)	12.2(1.26–33.8)
48	14.2(9.65–22.7)	4.31(0.496–15.3)	7.46(0.721–25.4)
60	12.0(8.58–19.2)	3.72(0.491–13.5)	6.52(0.600–22.3)
90	9.51(6.87–14.9)	2.82(0.410–10.8)	5.26(0.423–18.7)
120	8.16(6.09–12.7)	2.19(0.214–9.87)	4.32(0.333–15.5)

Values in ( ) are the maximum and minimum y^+, which is defined as $y^+=y\sqrt{\tau_w/\rho}/\nu 11$

The finite volume method was employed to discretize Eqs. (A1)–(A4). The pressure-velocity coupling equation was established by means of the SIMPLE algorithm. The pressure and velocity components were defined at a staggered mesh, i.e., the PRESTO (PRESsure STaggering Option) scheme was chosen in Fluent 6.3. The 2nd-order upwind scheme was selected for the convective terms in the momentum, kinetic energy and its dissipation rate equations, while the central difference scheme was applied to the dissipation terms in these equations.

At the suction pipe entrance, a velocity-inlet boundary condition was implemented along with 5% turbulence intensity and a 32 mm hydraulic diameter. The imposed normal velocity was calculated by the specified flow rate and the cross-section of the pipe. At the volute outlet, a zero-gauge pressure was imposed, and 5% turbulence intensity and 23 mm hydraulic diameter were specified. No-slip velocity boundary condition was activated at the walls with zero roughness.

The under-relaxation coefficients were set to 0.3, 0.5, 0.8 and 0.8 for the pressure-velocity coupling equation, momentum equations, turbulent kinetic energy, and its dissipation equations, respectively. The convergence criterion was defined as 1×10^{-5} for the residuals of these equations.

Whatever the mesh, the performance curves predicted with the 2nd-order up-wind scheme agree well with the experimental data. Thus, mesh2 and the 2nd-order up-wind scheme for the convective terms were applied in the simulations. The details of the independence of mesh size and validation against the experimental performance data are referred to in [43, 46] and ignored here.

Appendix B. One-Dimensional Hydraulic Loss Model

A 1D hydraulic loss model was composed based on various empirical correlations found in the literature. The model was used to obtain the pump head from the impeller theoretical head in the mean-line flow model. The model takes the hydraulic losses in the impeller, chamber, and volute into account. In the impeller, there are friction and diffusion losses, vortex loss (separate loss), and incidence loss. Here, the friction loss, diffusion loss and incidence loss h are considered because the vortex loss is too complex to be estimated. The formula for h is expressed with Eq. (7). The friction and diffusion loss h_{fd} can be estimated by considering each channel in the impeller as a straight plane diffuser and written as in [50]:

$$h_{fd}=Z\lambda_{fd}\frac{\overline{W}^2}{2g},\ \lambda_{fd}=3.2\left(tan\frac{\alpha}{2}\right)^{1.25}\left(1-\frac{A_1}{A_2}\right)^2+ \\ +\frac{\lambda_{fi}}{4sin\frac{\alpha}{2}}\left\{\frac{a_1}{b}\left(1-\frac{A_1}{A_2}\right)+0.5\left[1-\left(\frac{A_1}{A_2}\right)^2\right]\right\} \tag{B1}$$

where Z is the number of blades, Z=8, λ_{fd} is the flow resistance coefficient in a channel of the impeller, λ_{fi} is the friction factor in the channel, α is the expansion angle of the impeller, $\alpha=2\pi/Z$, A_1 is the inlet area of the channel, $A_1=ab$, a is the blade pitch in the inlet, $a_1=((2\pi R_1)/Z-\delta)$, δ is the blade metal thickness, δ=1.5 mm, A_2 is the outlet area of the channel, $A_2=a_2 b$, a_2 is the blade pitch in the outlet, $a_2=((2\pi R_2)/Z-\delta)$, $\overline{W}$ is the mean relative velocity in the channel, and is roughly the mean of the relative velocities in the inlet and outlet of the impeller, and R_{fd} is the Reynolds number of the channel and defined by:

$$R_{fd} = \frac{d_{hfd}\overline{W}}{\nu},\ d_{hfd} = 0.5\left(\frac{4a_1b}{2a_1+2b} + \frac{4a_2b}{2a_2+2b}\right) \tag{B2}$$

Prandtl's universal law of friction for smooth pipes in [51] was adopted to estimate λ_{fi} here. However, the law is an implicit function of λ_{fi} itself and inconvenient for use. The best curve fitting has to be conducted when the Reynolds number is in the range of 2×10^3–5×10^6, and the following explicit function of λ_{fi} is obtained:

$$\lambda_{fi} = 10^{-1.0463ln[log_{10}(R_{fd})]-5.9589\times10^{-2}} \tag{B3}$$

Friction loss exists at the side wall of the pump chamber. The chamber is considered a channel with a smooth side wall. The friction loss h_{ch} at the side wall is estimated with:

$$h_{ch} = \sum_{i=1}^{N} \lambda_{chi} \frac{2\pi R_i}{d_{hc}} \frac{V_{uchi}^2}{2g},\ R_{chi} = \frac{d_{hch}V_{uchi}}{\nu},$$
$$d_{hch} = 4B,\ V_{uchi} = 0.75V_{ui} \tag{B4}$$

where B is the width of the pump chamber, B=20mm, d_{hch} is the hydraulic diameter of the chamber, N is the number of the points employed to extract the fluid velocity profiles, R_i is the radii employed to extract the fluid velocity profiles, R_{chi} is the Reynolds number of the chamber, V_{uchi} is the mean fluid tangential velocity at R_i, V_{ui} is the fluid tangential velocity at R_i, and λ_{chi} is the friction factor and identical to that in Eq. (B3), and written as:

$$\lambda_{chi} = 10^{-1.0463ln[log_{10}(R_{chi})]-5.9589\times10^{-2}} \tag{B5}$$

There is friction loss and secondary flow loss in the volute body and there is friction loss and expansion loss in the discharge nozzle of the volute. The friction loss and secondary flow losses h_{vb} in the volute body are approximated by considering the volute body as a smooth bend, and expressed as [50]:

$$h_{vb} = \lambda_{vb} \frac{\theta_v R_m}{d_{hvb}} \frac{V_{vb}^2}{2g},\ d_{hvb} = \frac{4(R_4-R_3)b_3}{2b_3+(R_4-R_3)},$$
$$R_m = 0.5(R_4+R_3), \tag{B6}$$
$$V_{vb} = \frac{Q}{(R_4-R_3)b_3},\ R_{vb} = \frac{d_{hvb}V_{vb}}{\nu}$$

where θ_v is the warp angle, θ_v=350°, b_3 is the volute width, b_3=25 mm, d_{hvb} is the hydraulic diameter of the volute body, R_3 is the radius of the base circle of the volute, R_3=50 mm, R_4 is the radius of the volute body, R_4=70 mm, R_m is the mean radius of the volute body, V_{vb} is the mean velocity of fluid in the volute, and λ_{vb} is the friction and secondary flow loss coefficient in the volute body. λ_{vb} is determined by using the following empirical correlations [50]:

$$\lambda_{vb} = \begin{cases} \frac{20}{R_{vb}^{0.65}}\left(\frac{d_{hvb}}{2R_m}\right)^{0.175}, 50 < R_{vb} \le 600 \\ \frac{10.4}{R_{vb}^{0.55}}\left(\frac{d_{hvb}}{2R_m}\right)^{0.225}, 600 < R_{vb} \le 1400 \\ \frac{5}{R_{vb}^{0.45}}\left(\frac{d_{hvb}}{2R_m}\right)^{0.275}, 1400 < R_{vb} \le 5000 \end{cases} \tag{B7}$$

The nozzle of the volute is a short smooth tube with a rectangular cross-section. For this tube, the friction loss in it is calculated by the following expression [50]:

$$h_{vn} = \lambda_{vn} \frac{L_{vn}}{d_{hvn}} \frac{V_{vn}^2}{2g},\ d_{hvn} = \frac{4a_4b_4}{2a_4+2b_4},$$
$$R_{vn} = \frac{d_{hvn}V_{vn}}{\nu},\ V_{vn} = \frac{Q}{a_4b_4} \tag{B8}$$

where a_4 is the depth of the nozzle, a_4=21 mm, b_4 is the width of the nozzle, b_4=24 mm, d_{hvn} is the hydraulic diameter of the nozzle, L_{vn} is the length of the nozzle, L_n=60 mm, R_{vn} is the Reynolds number of the tube, V_{vn} is the mean velocity of the fluid in the tube, and λ_{vn} is the friction factor of the tube, and expressed by:

$$\lambda_{vn} = 10^{-1.0463ln[log_{10}(R_{vn})]-5.9589\times10^{-2}} \tag{B9}$$

After the various hydraulic losses mentioned above are determined, the pump head H is calculated by:

$$H = H_{th} - h_{fd} - h \quad - h_{ch} - h_{vb} - h_{vn} \tag{B10}$$

where the hydraulic losses h_{ch} and h_{vb} are more dominant than the losses h, h_{fd} and h_{vn}. Once the pump head is determined, the pump hydraulic efficiency is calculated with:

$$\eta_h = H/H_{th} \tag{B11}$$

where η_h is the pump hydraulic efficiency.

References

[1] Rütschi K 1968 *Die Arbeitsweise von freistrompumpen, Schweizerische Bauzeitung* **86** (32) pp. 575–582

[2] Ohba H, Nakashima Y, Shiramoto K, Shiramoto K and Kojima T 1983 *A study on internal flow and performance of a vortex pump: Part 2-a comparison between analysis and experimental results, and a design method of pump* Bulletin of JSME **26** (216) pp. 1007–1013

[3] Sha Y and Hou L 2010 *Effect of impeller location and flow measurement in volute of a vortex pump* Transactions of the Chinese Society for Agricultural Machinery, 2010, **41** (11) pp. 57–62

[4] Gerlach A, Thamsen P U, Wulff S and Jacobsen C B 2017 *Design parameters of vortex pumps: A meta-analysis of experimental studies* Energies **10** (58)

[5] Ohba H, Nakashima Y, Shiramoto K and Shiramoto K 1982 *On the performance of a vortex pump for solid-liquid fluid* Turbomachinery **10** (2) pp. 18–24

[6] Sha Y and Liu X 2013 *Performance test on solid-liquid two-phase flow hydrotransport of vortex pump* Transactions of the Chinese Society of Agricultural Engineering **29** (22) pp. 76–82

[7] Gerlach A, Perlitz D, Lykholt-Ustrup F, Jacobsen C B and Thamsen P U 2017 *The clogging behavior of a vortex pump - an experimental study on the influence of impeller designs* Proceedings of the ASME 2017 pp. 1–10

[8] Schivley G P and Dussourd J L 1970 *An analytical and experimental study of a vortex pump* ASME Journal of Basic Engineering **92** (4) pp. 889–900

[9] Ohba H, Nakashima Y, Shiramoto K, Shiramoto K and Kozima T 1978 *A study on performance and internal flow pattern of a vortex pump* Bulletin of JSME, 1978, **21** (162) pp. 1741–1749

[10] Aoki M 1983 *Studies on the vortex pump* (*1st report, internal flow*) Bulletin of JSME **26** (213) pp. 387–393

[11] Aoki M 1983 *Studies on the vortex pump (2nd report, pump performance)* Bulletin of JSME **26** (213) pp. 394–398

[12] Aoki M 1983 *Studies on the vortex pump (3rd report, estimation of pump performance)* Bulletin of JSME **26** (216) pp. 1014–1019

[13] Chen H 1996 *Measurement of rotating flow field within vortex pump* Transactions of the Chinese Society for Agricultural Machinery **27** (4) pp. 49–54

[14] Yang M, Gao B, Gu H and Li H 2008 *Measurement on 3D turbulent flow field in vortex pump* Drainage and Irrigation Machinery **26** (1) pp. 60–63

[14] Sha Y 2011 *Experiments on performance and internal flow of a vortex pump* Transactions of the Chinese Society of Agricultural Engineering **27** (4) pp. 141–146

[15] Kikuyama K, Murakami M, Minemura K, Asakura E and Ikegami T 1986 *The effects of entrained air upon a vortex pump performance* Transactions of JSME Series B, **52** (473) pp. 393–400

[16] Sha Y and Liu X 2014 *Numerical calculation on gas-liquid two-phase hydrotransport and flow field measurement in volute with probes for vortex pump* Transactions of the Chinese Society of Agricultural Engineering **30** (18) pp. 93–100

[17] Yang M, Gao B, Liu D, Gu H and Li H 2008 *Experimental investigation of salt-out two-phase flow in a vortex pump by PDPA measurements* Journal of Engineering Thermophysics **29** (2) pp. 237–240

[18] Yang M, Gao B, Liu D, Li H and Gu H 2007 *Analysis on liquid-solid two-phase flow field in a vortex pump by PDPA measurement* Transactions of the Chinese Society for Agricultural Machinery **38** (12) pp. 53–57

[19] Gao B and Yang M 2009 *Particle concentration distribution and its effect on salt-out features in a vortex pump* Journal of Engineering Thermophysics **30** (12) pp. 2031–2033

[20] Gao B and Yang M 2010 *Research on turbulent velocity fluctuations of salt-out particles in a vortex pump volute* Journal of Engineering Thermophysics **31** (2) pp. 275–278

[21] Ohba H, Nakashima Y and Shiramoto K 1983 *A study on internal flow and performance of a vortex pump: Part 1 theoretical analysis* Bulletin of JSME **26** (216) pp. 999–1006

[22] Chen H 1993 *A study on internal flow field in a vortex pump* Transactions of the Chinese Society for Agricultural Machinery **24** (2) pp. 24–27

[23] Chen H X 2004 *Research on turbulent flow within the vortex pump* Journal of Hydrodynamics Series B **16** (6) pp. 701–707

[24] Shi W, Wang Y, Kong F, Sha Y and Yuan H 2005 *Numerical simulation of internal flow field within the volute of vortex pump* Transactions of the Chinese Society of Agricultural Engineering **21** (9) pp. 72–75

[25] Xia P, Liu S and Wu Y 2006 *Numerical simulation of steady flow in vortex pump* Journal of Engineering Thermophysics **27** (5) pp. 420–422

[26] Shi W, Wang Y, Sha Y, Liu H and Wang Z 2006 *Research on the internal flow of vortex pump* Transactions of the Chinese Society of Agricultural Engineering **37** (1) pp. 47–50

[27] Tan P, Sha Y, Bai X, Tu D, Ma J, Huang W and Fang Y 2017 *A performance test and internal flow field simulation of a vortex pump* Applied Sciences **7** pp. 1273

[28] Gerlach A, Preuss E, Thamsen P U and Lykholt-Ustrup F 2017 *Numerical simulations of the internal flow pattern of a vortex pump compared to the Hamel-Oseen vortex* Journal of Mechanical Science and technolog **31** (4) pp. 1711–1719

[29] Quan H, Chai Y, Li R and Guo J 2019 *Numerical simulation and experiment for study on internal flow pattern of vortex pump* Engineering Computations **36** (5) pp. 1579–1596

[30] Quan H, Chai Y, Li R, Peng G Y and Guo Y 2019 *Influence of circulating-flow's geometric characters on energy transition of a vortex pump* Engineering Computations **36** (9) pp. 3122–3137

[31] Zhao K, Liu H, Du Z, Tan M, Hu S and Dong L 2021 *Analysis of flow loss characteristic of vortex pump based on entropy production* Journal of Drainage and Irrigation Machinery **39** (12) pp. 1285–1290

[32] Quan H, Cheng J, Guo Y, Kang L and Peng G 2020 *Influence of screw centrifugal inducer on internal flow structure of vortex pump* ASME Journal of Fluids Engineering **142** (9) p. 091203

[33] Cervinka M 2012 *Computational study of sludge pump design with vortex impeller* Proceedings of 18th International Conference on Engineering Mechanics pp. 191–201

[34] Gao X, Shi W, Zhang D, Zhang Q and Fang B 2014 *Optimization design and test of vortex pump based on CFD orthogonal test* Transactions of the Chinese Society for Agricultural Machinery **45** (5) pp. 101–106

[35] Quan H, Guo Y, Li R, Su Q and Chai Y *Optimization design and experimental study of vortex pump based on orthogonal test* Science Progress **103** (1) pp. 1–20

[36] Chen H X, Shi F and Guo J H 2006 *Numerical research on the three-dimensional unsteady flow within the vortex pump* International Journal of Turbo and Jet Engines **23** (1) pp. 27–35

[37] Yang M, Gao B, Li H and Gu H 2008 *Simulation and experimental research on salt-out two-phase flow field in a vortex pump* Journal of Mechanical Engineering **44** (12) pp. 42–48

[38] Gao X, Shi W, Shi Y, Chang H and Zhao T 2020 *DEM-CFD simulation and experiments on the flow characteristics of particles in vortex pumps* Water **12** p. 2444

[39] Quan H, Kang L, Guo Y, Cheng J, Yu X, Quan S 2021 *Effect of solid concentration on circulation flow and hydraulic characteristics in vortex pump* Journal of Drainage and Irrigation Machinery **39** (6) pp. 555–561

[40] Quan H, Li Y, Kang L, Yu X, Song K and Wu Y 2021 *Influence of blade type on the flow structure of a vortex pump for solid-liquid two-phase flow* Machines **9** p. 353

[41] Imasaka Y, Kanno H, Saito S, Miyagawa K, Nohmi M, Isono M and Kawai M 2018 *Clogging mechanisms of vortex pumps: Fibrous material motion capture and simulation with a CFD and DEM coupling method* Proceedings of the ASME 2018 5th Joint US-European Fluids Engineering Division Summer Meeting pp. 1–10

[42] Steinmann A, Wurm H and Otto A 2010 *Numerical and experimental investigations of the unsteady cavitating flow in a vortex pump* The 9th International Conference on Hydrodynamics

[43] Li W and Zhang Y 2018 *The vortex pump under highly viscous liquid flow conditions* Arabian Journal for Science and Engineering **43** pp. 4739–4761

[44] Quan H, Yu X, Li Y, Song K, Pu H and Wang W 2021 *Influence of liquid viscosity on internal flow structure in vortex pumps* Journal of Drainage and Irrigation Machinery **39** (12) pp. 1278–1283

[45] *Fluent Inc, FLUENT 6.2 User's Guide, Volume 1 and 2* 2005 Fluent Inc, Lebanon

[46] Li W 2022 *Vortex pump as turbine for energy recovery in viscous fluid flows with Reynolds number effect* ASME Journal of Fluids Engineering **144** (2) p. 021207

[47] Veres J P 1994 *Centrifugal and Axial Pump Design and Off-Design Performance Prediction, NASA TM-106745* pp. 1–22

[48] El-Naggar M A 2013 *A one-dimensional flow analysis for the prediction of centrifugal pump performance characteristics* International Journal of Rotating Machinery **2013** pp. 1–19, doi:10.1155/2013/473512

[49] Steponoff A J 1957 *Centrifugal and Axial Flow Pumps* (*2nd edition*) Krieger Publishing Company, Malabar

[50] Idelchik I E 1968 *Handbook of Hydraulic Resistance* Israel Program for Scientific Translations Ltd, Jerusalem

[51] Schlichting H 1979 *Boundary-Layer Theory* (*7th edition*) McGraw-Hill Book Company, New York

[52] Gerlach A, The Influence of Impeller Designs on the Performance of a Vortex Pump, PhD Thesis: Technical University of Berlin, Berlin, Germany, 2018

[53] Kondus V Y, Puzik R V, German V F, Panchenko V O and Yakhnenko S M 2021 *Improving the efficiency of the operating process of high specific speed torque-flow pumps by upgrading the flowing part design* Journal of Physics: Conference Series **1741** p. 012023

[54] Gao X, Zhao T, Shi W, Zhang D, Shi Y, Zhou L and Chang H 2020 *Numerical investigation of an open-design vortex pump with different blade wrap angles of impeller* Processes **8** p. 1601

[55] Dai L, Gu L, Wang J, Ao X and Zhu X 2020 *The effect of impeller indent distance on the performance of vortex pumps* International Journal of Fluid Machinery and Systems **13** (1) pp. 42–54

[56] Panchenko V, German V, Kondus V, Ivchenko O and Ryasnaya O 2021 *Combined operating process of torque flow pump* Journal of Physics: Conference Series **1741** p. 012022

[57] Jiang D, Lv J, Dai L and Su B 2012 *Numerical simulation of and experimental research on optimum efficiency of vortex pumps* China Rural Water and Hydropower **4** pp. 92–94

[58] Gerlach A, Thamsen P U and Lykholt-Ustrup F 2016 *Experimental Investigation on the Performance of a Vortex Pump using Winglets* International Symposium on Transport Phenomena and Dynamics of Rotating Machinery pp. 1–6

[59] Zhu R, Su B, Wang X and Yin Y 2010 *Numerical simulation and experiment of influence of hem on performance of vortex pump* Journal of Drainage and Irrigation Machinery Engineering **28** (5) pp. 398–401

[60] Machalski A, Skrzypacz J, Szulc P and Błoński D 2021 *Experimental and numerical research on influence of winglets arrangement on vortex pump performance* Journal of Physics: Conference Series **1741** p. 012019

[61] Wang X, Zhu R, Yu Z and Su B 2011 *Influence of high-low blade on performance of vortex pumps* China Mechanical Engineering **22** (17) pp. 2030–2033